Manuscript prepared for The Cryosphere
with version 4.2 of the LATEX class copernicus.cls.
Date: 28 March 2014

Two independent methods for mapping the grounding line of an outlet glacier; example from the Astrolabe Glacier, Terre Adélie, Antarctica

E. Le Meur[1,2], M. Sacchettini[1,2], S. Garambois[3], E. Berthier[4], A. S. Drouet[1,2], G. Durand[1,2], D. Young[5], J. S. Greenbaum[5], D. D. Blankenship[5], J. W. Holt[5], E. Rignot[6,7], J. Mouginot[6], Y. Gim[7], D. Kirchner[8], B. de Fleurian[1,2], O. Gagliardini[1,2,9], and F. Gillet-Chaulet[1,2]

[1]CNRS, LGGE (UMR 5183), F-38041 Grenoble, France
[2]Univ. Grenoble Alpes, LGGE (UMR 5183), F-38041 Grenoble, France
[3]ISTerre, UJF-Grenoble, CNRS, Saint Martin d'Hres, France
[4]LEGOS, CNRS, Universit de Toulouse, Toulouse, France
[5]Institute for Geophysics, University of texas, Texas, USA
[6]Earth System Science, University of California, Irvine, California, USA
[7]Jet Propulsion Laboratory, California, Institute of Technology, Pasadena, California, USA
[8]University of Iowa, Dept. of Physics and Astronomy, Iowa city, IA , USA
[9]Institut Universitaire de France, Paris, France

Abstract. The grounding line is a key element acting on the dynamics of coastal outlet glaciers. Knowing its position accurately is fundamental for both modelling the glacier dynamics and establishing a benchmark to which one can later refer in case of change. Here we map the grounding line of the Astrolabe Glacier in East Antarctica ($66°41'S$;$140°05'E$), using hydrostatic and tidal methods. The first method is based on new surface and ice thickness data from which the line of buoyant flotation is found. We compare this hydrostatic map with kinematic GPS measurements of the tidal response of the ice surface. By detecting the transitions where the ice starts to move vertically in response to the tidal forcing we determine control points for the grounding line position along GPS profiles. With the help of a 2-dimensional elastic plate model, the rigid short-term behaviour of the ice plate is computed and allows estimates of the required correction to apply to the kinematic GPS control points in order to compare them to the previously determined line of floatation. These two approaches show consistency and lead us to propose a grounding line for the Astrolabe Glacier that significantly deviates from those obtained so far from satellite imagery.

1 Introduction

For glaciers and ice-streams draining ice sheets to the sea, the transition between the inner grounded ice and its outer floating counterpart defines the so-called Grounding Line (GL). This line represents a fundamental transition in ice dynamics, separating two drastically different ice flow regimes, shear-dominant flow for the grounded part and a longitudinal stress-dominant one for the floating shelf (see for instance Pattyn et al. (2006)). Proper demarcation of the GL is required for determining appropriate model discretization and mechanical equations (Durand et al. (2009), Schoof (2007)).

Correspondence to: Emmanuel Le Meur
(lemeur@lgge.obs.ujf-grenoble.fr)

A second issue is that the contribution of continental ice sheets to sea level is determined by when ice passes through the grounding line and becomes afloat. As a consequence, any ice flow budget over outlet glaciers requires proper knowledge of ice thickness at the location of the GL and preferably slightly upstream given the high melting rates encountered in the vicinity and downstream of the grounding line (Depoorter et al., 2013). Considering ice thickness far downstream of the GL can significantly underestimate the ice flux given the importance of mass exchange (mainly melting) between the floating ice and the ocean (see for instance Gagliardini et al. (2010), Rignot and Jacobs (2002), Joughin and Padman (2003)). Given the availability of ice surface velocities over floating ice (Rignot et al. (2011), Joughin et al. (1998)) and a low vertical velocity gradient due to no basal drag on the floating ice, accurate computations of the ice flux close to the grounding line are now becoming possible (Shepherd et al., 2012).

In this paper we carefully evaluate two methods for locating the grounding line using Astrolabe Glacier in East Antarctica's Terre Adélie as a test case. Astrolabe Glacier lies immediately next to the French Dumont d'Urville Station (see location on Fig. 1), and thus has been uniquely accessible for a range of geophysical investigations. Using a diverse range of ground, airborne and spaceborne data, we constrain at intermediate resolution the grounding line of Astrolable Glacier using hydrostatic and tidal methods.

2 Methods for locating the grounding line

There has been numerous large-scale attempts for delineating the GL around Antarctica using various ground, air or spaceborne techniques. The identification of the GL is complicated by the finite elastic properties of ice, which spreads

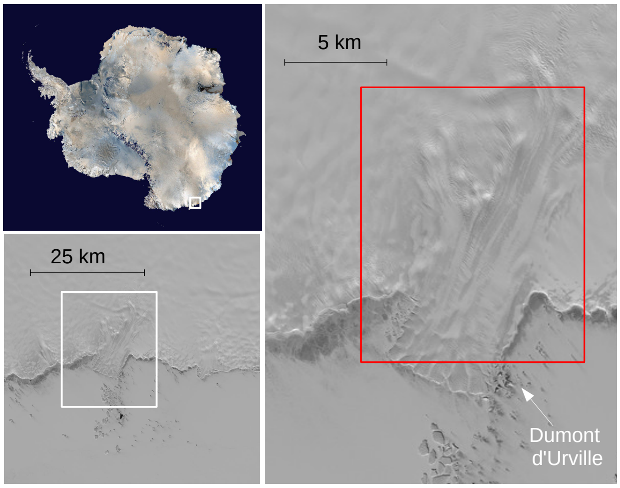

Fig. 1. Location of the Astrolabe Glacier in the Terre Adelie sector of East Antarctica from a AVHRR global picture (upper left). The lower left regional view as well as the focus on the coastal part of the glacier (right) come from a SPOT HRG1 image taken on the 28 November 2003 (©CNES / Distribution Spot Image). The red square shows the location of Fig. 4.

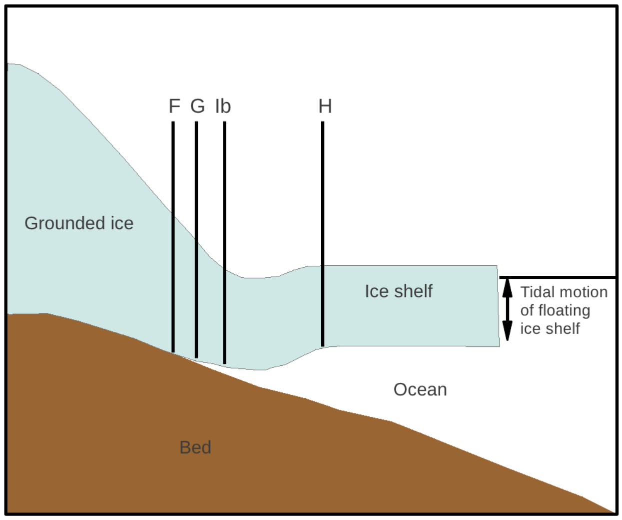

Fig. 2. Important points along the transition between grounded and floating ice. F represents the landward limit of tidally-induced vertical displacements, G the grounding line where the ice bottom actually splits from the ground, Ib the so called 'break in slope' and H the limit where the rigid effects of the elastic bending of the ice slab do not propagate any further, allowing the ice to freely float on the ocean, (adapted from Brunt et al. (2010)).

the surface expression of the GL out into a wider Grounding Zone (GZ). The GZ feature most widely mapped is I_b (see Fig. 2 adapted from that of Brunt et al. (2010)), a characteristic slope break thought to represent change from basal drag to no basal drag. However, additional features of the GZ relating to ocean dynamics and buoyancy provide a more direct proxy of the ice-rock separation.

Buoyancy considers the ice slab in its long-term interaction with an 'averaged non-tidal' ocean under the form of a predominantly viscous deformation when the ice comes to floatation (see Fig. 3). As the result , transmission of rigid stresses is reduced allowing for the use of the hydrostatic approach in a first determination of the GL.

On the other hand, tidally-induced changes in the ice upper surface can be recorded to provide a dynamical proxy for the GL from the limit between mobile and immobile upper surface areas. Over the shorter-term forcing of the tides (hourly to daily), rigid stresses become more pronounced (the ice behaving more elastically (Vaughan, 1995)), which leads to a regional tidal flexure of the plate all over the F-H distance (see Fig. 3). F is the landward limit of the ice upper deformation under tidal forcing whereas H is the seaward limit of the rigid effects where free floatation is recovered (Fricker and Padman, 2006). The contact point (ice-rock separation) moves from point G_H at high tide to point G_L seaward of the G point at low tide. An alternative for the GL positioning therefore consists of considering the line of F points which undergo the first vertical displacements at the ice upper surface (see figure). Points actually mapped (X points) will then lie seaward, all the closer to the F point as the detection threshold of the kinematic method used is small (for instance 10 to 20 cm with ICESat laser altimetry (Fricker and Padman, 2006) or less than $1cm$ with differential satellite synthetic aperture radar interferometry (DInSAR, Rignot et al. (2011)). The figure is complicated by the rigid tilting of the slab which exerts a bending moment that lifts the outer fringe whilst still maintaining the ice more or less in contact with the bedrock. The resulting F-G offset (more specifically the X-G offset) is therefore responsible for the difference between an hydrostatic and a kinematic grounding line determination. Modelling the tidally induced flexure of the ice slab is a way of assessing these distances and hence the consistency between the hydrostatic and kinematic approaches as carried out in the present study. The three approaches for mapping the grounding line (the hydrostatic method, the tidal method and the surface slope method) allow identification of GZ features. Combining these methods helps define the GL location.

2.1 Hydrostatic Methods

Hydrostatic methods use Archimedes' Principle to estimate from surface elevation data the ice thickness required for a column of ice to float; this estimate is compared to measured ice thickness data to calculate "floatation" (Robin et al., 1983; Corr et al., 2001). Where the two numbers are the same, the ice is floating. Errors in this method come from the neglection of rigid internal stresses within the ice slab, from errors in surface elevation, in the value of the ice-water density contrast, and in the surface elevation as well as in ice thickness estimates.

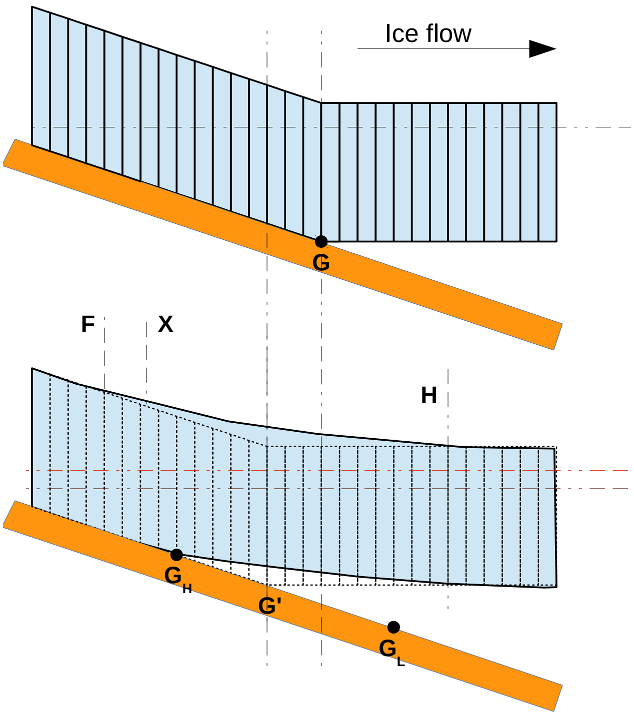

Fig. 3. Ice ocean interactions near the grounding line. The top of the figure represents the grounded/floating transition for an outlet glacier where hydrostatic equilibrium with a constant 'non-tidal' ocean is assumed throughout. The lack of rigid stresses is here illustrated by blocks floating independently from one another. The floatation criterion allows a first estimation of the contact point G. The situation as depicted on top is supposed to represent an average sea level between low and high tides. The bottom of the figure now considers the effects of the tidal rise (red line) superposed on top of the previous reference state. Should the response remain purely hydrostatic, tidal deformation would only span the GG' distance therefore representing an underestimated migration of the grounding line. In fact, the tidally short term forcing implies a rigid behaviour making the deformation spread over the entire grounding zone (FH) now implying a more realistic migration for the grounding line. As a result, ice surface movements are to be expected from F and will become detectable after a certain distance seaward (at point X) depending on the detection threshold of the kinematic method used.

2.2 Tidal Methods

Tidal methods consist of tracking time-dependent surface elevation changes generated by the tides (e.g. Fricker and Padman (2006)). Synthetic Aperture Radar Interferometry (InSAR) has been widely employed for mapping the 2-D time-dependent vertical displacement field in response to tidal forcing (Rignot (1998), Goldstein et al. (2013)). Usually the line of F points is considered as a good representation of the GL, the difference between different studies comes from different detection thresholds in the measurement method leading to various downflow shifts in the points actually measured. Because of a very low noise level for their DynSAR method (less than a cm vertical displacement), Rignot et al. (2011) obtain a detectable tidal signal shortly after the F line (before the G point) which they consider as the true GL. However, due to the narrowness of the F-G distance over Petermann glacier (500 m to 1 km, (Rignot et al., 2011)), mapping G of F does not make a big difference in the present case.

Similarly to InSAR, ice surface elevation temporal changes have also been assessed from ICESat repeat-track altimetry at different tidal phases (see for instance Fricker and Padman (2006); Brunt et al. (2010) and references therein), the main limitation being a discrete number of tracks that only cross the grounding line at points spaced 10 km along much of the Antarctic coast. The method here also theoretically maps the inner limit of surface deformation (F points), but a much larger noise level certainly induces larger offsets towards G for the points actually detected. H points (full floatation recovery) are also mapped giving the grounding zone width (F-H). Contrary to Petermann glacier, much larger grounding zones are found with an average width of 3.2 km (2.6 km standard deviation) sometimes exceeding 10 km for the study area of Brunt et al. (2010) on the Ross ice shelf . The considered true grounding line G lying somewhere in between, it is sometimes difficult to assess the accuracy of the proposed positioning. However, large grounding zones often characterize large outlet glaciers for which uncertainty of the order of the km in the proposed kinematic methods still provides a refinement in the grounding line position compared to earlier mappings from different satellite methods (Fricker and Padman (2006), Brunt et al. (2010)).

2.3 Surface slope Methods

Surface slope methods rely on the identification of small scale surface topographic features from visible satellite imagery or a Digital Elevation Model (DEM). These features comprise flow stripe disruption, surface manifestation of basal crevasses or a break in the surface slope (I_b) all of which are inferred to appear when the ice starts to float (Brunt et al., 2010). Scambos et al. (2007) used a constrained range of sun illumination (optimized for the expression of surface slopes) in the MODIS Mosaic image of Antarctica allowing for the determination of the break-in-slope (I_b) to infer a grounding line location. Horgan and Anandakrishnan (2006) used a surface slope analysis from a high resolution DEM derived from ICESat data. Bindschadler et al. (2011) used a surface slope method combining optical imagery (Landsat) with sparse ICESat altimetry for mapping the seaward limit of grounded ice features which best corresponds to I_b and constitutes their Antarctic Surface Accumulation and Ice Discharge (ASAID) GL. Bindschadler et al. (2011) provided a low resolution version of H, the limit at which ice is freely floating, using a tidal analysis of the sparse ICESat data.

2.4 Differences in results

Tidal and hydrostatic methods appear to provide a more reliable determination of the GL, but are temporally and spatially limited by data availability. Surface slope methods on the other hand can use a satellite imagery data record that extends back more than thirty years, and is not limited by decorelation due to environmental effects. In particular, this paper represents the first mapping of the Astrolabe Glacier grounding line using tidal methods, as this area was a gap in the Rignot et al. (2011) tidal grounding line dataset.

Rignot et al. (2011) find that their grounding line mapping obtained from differential satellite synthetic-aperture radar interferometry can deviate from that resulting from identification of the break-in-slope by as much as several tens of km, especially on fast moving outlet glaciers. Conversely, on more stagnant and slow-moving ice, tidal and surface slope methods better agree. As a tidal approach, the approach of Rignot et al. (2011) is consistent with those based on ICESat data, the main difference being a continuous mapping along the grounding line and a much lower detection noise (vertical motion measured with less than a centimeter precision).

In the present paper, after justifying the approach, a first position of the GL of Astrolabe Glacier is obtained from new bedrock and ice surface elevation data by applying an hydrostatic criterion. A ground based tidal approach, using kinematic GPS measurements of the tidally-induced displacement pattern of the ice slab is then used for inferring vertically moving and immobile areas of the glacier. With the help of a 2-D elastic rigid flexure model, the consistency between the two approaches is verified. A reliable grounding line positioning at intermediate resolution is then proposed for comparisons with published GL locations using the surface slope criterion.

3 Hydrostatic grounding line position

Assuming an average density ρ_i for the ice column, a theoretical floatation depth P can easily be computed from the ice upper elevation above sea level h according to :

$$P = \frac{\rho_i h}{\rho_w - \rho_i} \tag{1}$$

with ρ_w a sea water density of $1028\ \mathrm{kg.m^{-3}}$ (Craven et al., 2005). Comparison of this depth with the depth of the ice bottom obtained from radar soundings indicates whether the ice is freely floating or is grounded.

3.1 Ice upper surface

The ice upper elevation above sea level used for computing the hydrostatic profiles has been obtained from a 40-m digital elevation model (DEM) available for the entire Astrolabe Glacier. Surface heights were calculated from a pair of stereoscopic images acquired on the 14^{th} of December 2007 by the SPOT5-HRS sensor in the framework of the SPIRIT (SPOT 5 stereoscopic survey of Polar Ice: Reference Images and Topographies) IPY project (Korona et al., 2009).

We validate the vertical accuracy of the SPIRIT DEM using Release 33 ICESat-1 data acquired during laser period 3I (Zwally et al., 2005), on average 54 days before the acquisition date of the SPOT-5 stereo pair. Before comparison, ICESat-1 elevation are converted to altitude above the EGM96 geoid to match the datum of the SPIRIT DEM. For each ICESat footprint, the corresponding DEM elevation was extracted by bilinear interpolation.

When correlation artifacts are discarded using the correlation mask provided with the elevation dataset, the mean vertical bias is $-0.3\ \mathrm{m}$ (standard deviation $2.9\ \mathrm{m}, N = 2319$). For the part of the Astrolabe Glacier studied here (close and downstream of the grounding line), there are very few interpolated pixels because the glacier surface is highly crevassed (feature rich) and SPOT5 images have a good radiometric dynamic. Thus, $\pm 3\ \mathrm{m}$ is used as uncertainty for the elevation of the ice surface.

3.2 Ground penetrating radar survey

The Astrolabe Glacier has been the target of several recent radar campaigns with an emphasis on the coastal part of the glacier (Fig. 4). Ground Penetrating Radar (GPR) measurements were acquired along several-km long profiles with a MALÅ® ProEx GPR system connected to a $50\ \mathrm{MHz}$ Rough Terrain Antenna, which was towed by the operator on the ground. Measurements were acquired with a common offset of $4\ \mathrm{m}$ between the transmitter and the receiver antennas. The acquisition triggering, which was fixed to $5\ \mathrm{m}$ for all profiles, was automatically controlled using a calibrated encoder wheel and then repositioned thanks to GPS measurements, which allow deriving topography information. Data were acquired with a sampling frequency of $648\ \mathrm{MHz}$ over a 12.8 µs time window, and stacked 32 times.

The GPR data were processed using the Seismic Unix software (www.cwp.mines.edu /cwpcodes). The processing sequence includes time zero corrections and dewow zero-phase low-cut filter to remove direct continuous currents. In order to improve signal to noise ratio of late arrivals, a zero-phase band-pass filter was also applied to raw data in the $[30-70\ \mathrm{MHz}]$ frequency range. The data were then migrated using a Stolt f-k migration algorithm with a constant velocity of $168\ \mathrm{m.µs^{-1}}$ in order to correctly locate dipping events and to focus scattering hyperbolas. Finally, for display purposes, topographic corrections and time to depth conversions were computed using the same constant velocity.

This classical velocity in cold ice was measured outside of the glacier with Common Mid-Point (CMP) analyses. No firn correction is accounted for, given the fact that the ground radar measurements were almost entirely performed on the lower part of the glacier where accumulated snow is gener-

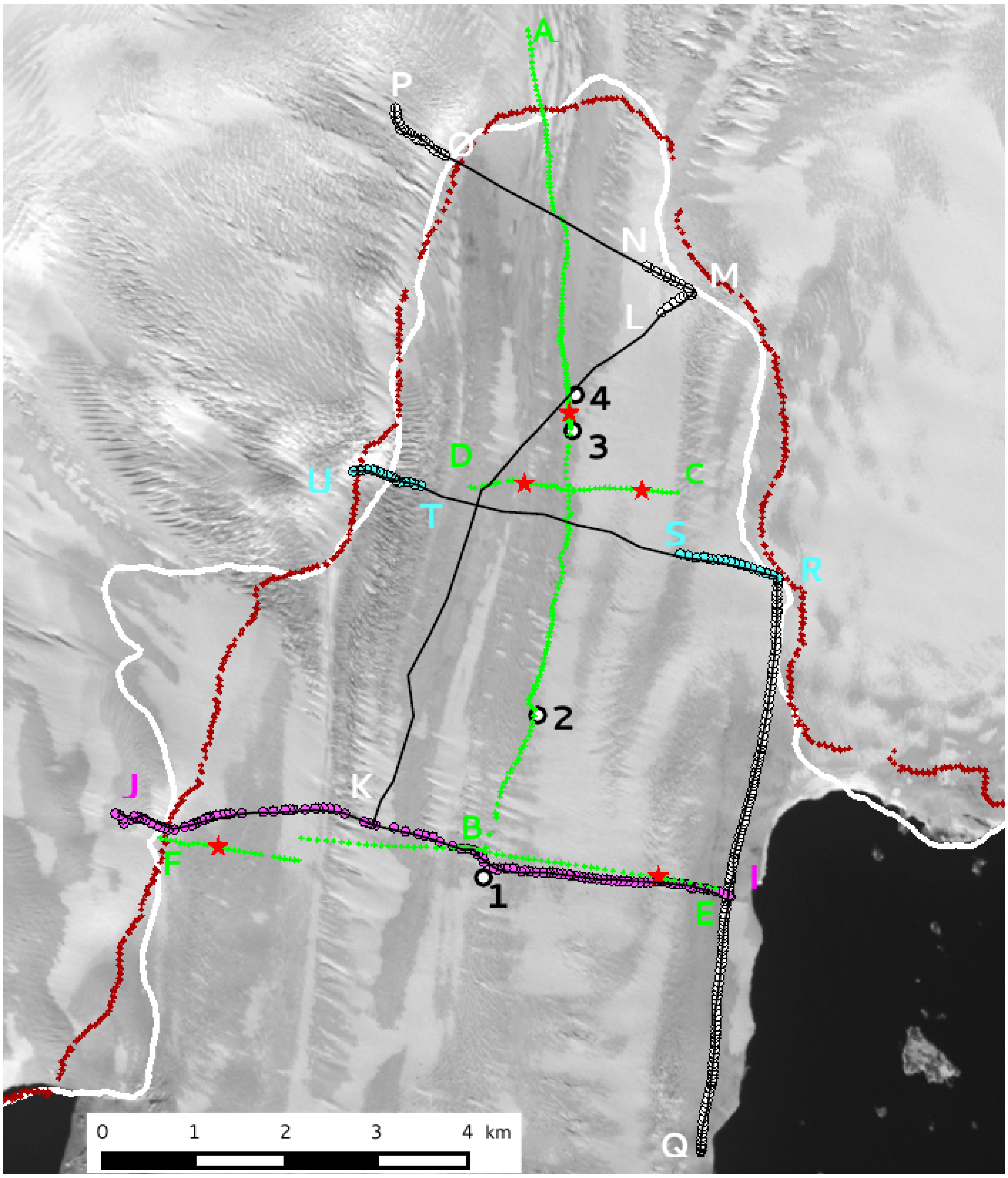

Fig. 4. Summary map of field activities deployed from the ground carried out on the Astrolabe Glacier superimposed on a ASTER Image. The thin black line outlines the ground radar profiles actually measured and the overlapping coloured dots the points where the ice bottom echo was detectable allowing for a depth to be inferred. Green dots represent each of the points measured twice by kinematic GPS in order to measure a difference in ice surface elevation between low and high tides and red crosses the resulting 'GPS control points' (see Sect. 4.1). Points 1 to 4 are the points where surface elevation was continuously monitored by GPS for several days (Sect. 4.2.2). Last, the white and brown lines are the grounding lines proposed by respectively Bindschadler et al. (2011) and Scambos et al. (2007).

ally turned into ice by the summer melting events that occur there (except over the uppermost part of profile QR, see Fig. 5). As topography variations are relatively smooth compared to penetration depth, topography corrections have been computed after migration. A gain was also applied to the data to compensate spreading signal attenuation.

Surface crevasses (seen from surface morphology (Fig. 4) and radargrams (middle of Fig. 5)) can corrupt the transmitted signal. As a result, ice thickness could only be assessed over some portions of the radar lines (black lines on Fig. 4, coloured dots show ice thickness observations). For the middle of Profile IJ, the inferred ice thicknesses should be considered with caution in the central part given the extreme weakness of the reflectors. Fig. 5 shows processed radar-

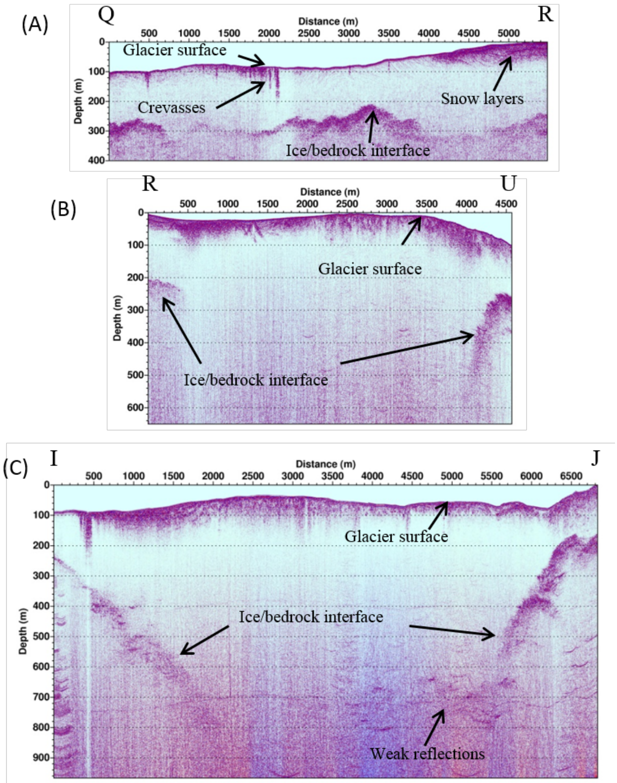

Fig. 5. Ice-bedrock interface measured by GPR along profiles QR (A), RU (B), and IJ (C) of Fig. 4. Snow layers horizons become visible on the QR profile after a distance of $4000\ \mathrm{m}$ when entering the accumulation zone. Combined effects of depth and floating ice seriously alter the reflectors in the middle of the IJ profile and lead to a total loss in the middle of the RU profile

grams corresponding to profiles QR, RU and IJ (see Fig. 4 for their respective locations).

On profile QR (Fig. 5 top), the basal interface is clearly visible as a strong unique reflector along the full profile due to thin ice ranging from 100 to $200\ \mathrm{m}$ on the grounded right hand side of the glacier. On profile IJ (Fig. 5 bottom) and profile RU (Fig. 5 middle), the basal interface is lost along the centerline of the glacier. This data gap could be due to the penetration limit of the GPR or to a decline in bed reflectivity. Indeed, weak focused hyperbolas are visible on the right part of profile IJ that may be resulting from the rough contact arising when the ice becomes afloat (Vaughan et al., 2012). This roughness in the basal interface could be due to salt water intrusions into bottom crevasses and cracks that creates large scattering hyperbolas that are not visible at the ice/bedrock interface (Van der Veen, 1998). Accretion and/or intrusion of marine ice can also be an explanation. For profile RU, the loss of signal in the central part is abrupt and occurs at different depths, $200\ \mathrm{m}$ on the left and $500\ \mathrm{m}$ on the right despite post-processing attempts to improve the signal-to-noise ratio.

3.3 Hydrostatic profiles

From the upper ice elevation along radar profiles where the ice bottom reflector can be unambiguously identified (coloured dots on Fig. 4), Eq. 1 is used to compute the corresponding theoretical profiles of floatation depths. A density of $1028\ \mathrm{kg.m^{-3}}$ is commonly accepted for sea water (Craven et al., 2005). Ice density is less well constrained. Various studies dealing with Antarctic ice shelves (Fricker et al., 2001; Wen et al., 2007, 2010) suggest a column-integrated ice density ranging from 880 to $900\ \mathrm{kg.m^{-3}}$ whereas Bamber and Bentley (1994) find a good fit in the comparison of satellite altimetry and ice thickness measurements with a higher value of $917\ \mathrm{kg.m^{-3}}$. In the present case, two factors contribute to a short-scale spatial variability of the ice column average density. By creating voids up to 40 m deep, crevassing, which in some places can be very intense (shear zones for instance), significantly reduces the overall density. On the other hand, the lack of firn in the central lower part of the glacier due to the entire melting of the snow by the end of the summer (ablation zone) is responsible for density values locally close to that of pure ice ($917\ \mathrm{kg.m^{-3}}$). It was therefore decided to adopt a central value of $890 \pm 10\ \mathrm{kg.m^{-3}}$ for our theoretical floatation computations.

Resulting profiles are depicted on Fig. 6. By denoting the bottom of the ice slab, the radar reflector is normally either above floatation (grounded ice), or lying within the floatation error bars (ice floating or close to be so). As indicated by the error bars, floatation depth uncertainties are sensitive to the ice density range. Assuming that hydrostatism is valid, meaning that the floatation curve cannot lie above the bedrock, these profiles allow for assessing a lower bound on the density value. Along profile TU for instance where floatation seems to be met except maybe at the very right hand side of the profile, one can see that density values can hardly go below $880\ \mathrm{kg.m^{-3}}$, lower values would significantly rise the floatation above the bedrock. A closer look shows that the lower-lying left side of the profile seems to favour higher densities (around $900\ \mathrm{kg.m^{-3}}$) whereas the upper one gives a better match with the top of the error bars ($880\ \mathrm{kg.m^{-3}}$) before grounding probably occurs at the very end. This is compatible with a gradient in the firn layer thickness from the lower central part up to the upper sides of the glacier. Similarly, Profile IJ tends to indicate higher density values in its central floating part with a better match with the bottom of the error bars ($900\ \mathrm{kg.m^{-3}}$). This again can be linked to the fact that the entire profile appears to be deprived of firn. Caution should however be considered especially with the central part of Profile IJ where the bottom depths result from a partly subjective interpretation of very faint reflectors. There is also a potential uncertainty on the depths deduced from the travel time of the electro-magnetic radar wave, but the observed lack of firn along most of the profiles led us to use the commonly accepted velocity value of $168\ \mathrm{m.\mu s^{-1}}$ for ice. This is confirmed by the excellent

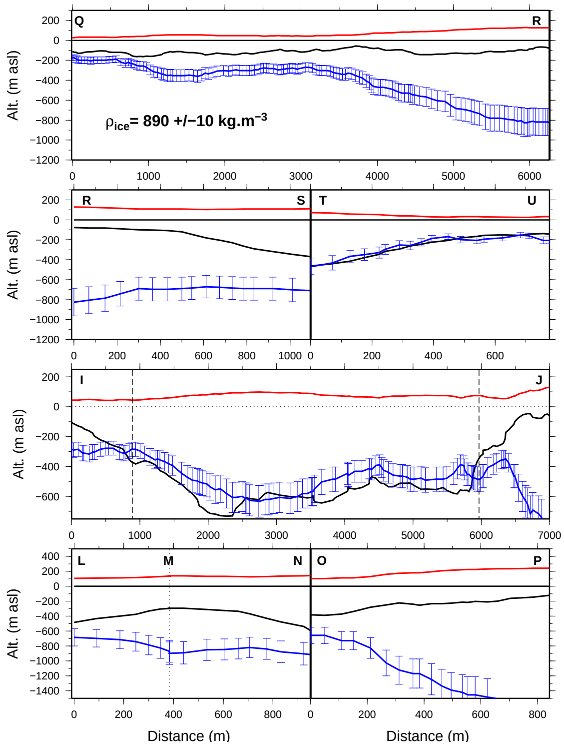

Fig. 6. Theoretical hydrostatic floatation depth (blue curve with error bars) computed with an ice density of $890 \pm 10\ \mathrm{kg.m^{-3}}$ compared to the ice bottom depth (black curve) inferred from Ground Penetrating Radar operated from the ground. The red curve represents the geoidal altitude of the ice upper surface obtained from the SPIRIT DEM. The profiles correspond to the coloured dots on Fig. 4. The vertical dashed lines on profile IJ show the location of to the 2 control points for the grounding line position obtained from the GPS kinematic method, (see Sect. 4.1).

match obtained with two boreholes down to the bedrock performed in the close vicinity (with one along the QR profile) which reached the depths of 153 and 296 m where ground radar profiles performed beforehand respectively gave 150 and 300 m. Therefore, only slight systematic deviations are to be expected from a possible error on the wave velocity. Plotting error bars on ground radar data is thus meaningless here as they mainly result from reflector misinterpretation over poorly resolved areas.

In some cases however, radar reflectors significantly above the theoretical floatation depth are a clear indicator of grounded ice like for instance along profiles QR, LN, OP and RS. Conversely, a good match between profiles (for example profile T-U) most probably indicates ice which is at or near floatation (except maybe at its very eastern end). Last, along profile IJ we find grounded ice in its outer parts, which then becomes afloat (or partly grounded) in its central part. Based on these results, areas of respective grounded and potentially floating ice for the GZ of Astrolabe Glacier can already be proposed and later refined with the help of extra airborne radar profiles.

3.4 Supplementary airborne radar data

As part of a collaborative project with the Jet Propulsion Laboratory (Warm Ice Sounding Explorer, WISE) and the University of Texas (International Collaborative Exploration of the Cryosphere for Airborne Profiling, ICECAP, Young et al. (2011)), several airborne geophysical campaigns have been undertaken during the 2008/09, 2009/10 and 2011/12 seasons in order to characterize some of the large outlet glaciers of the Wilkes Land - Terre Adélie sector of East Antarctica. Some of the flights were dedicated to the Astrolabe Glacier over which bedrock topography was measured with a combination of medium ($2.5\ \mathrm{MHz}$) (MF) and very high ($60\ \mathrm{MHz}$) frequency (VHF) high power sounding radars mounted on either a DHC-8 Twin Otter or a DC-3T Basler aircraft. Figure 7 shows one of the MF radar profile obtained over the glacier along the Y1-Y2 profile as represented on Fig. 8. A treatment similar to that applied to ground radar data was performed and allowed for similar theoretical hydrostatic floatation profiles as those depicted on Fig. 6.

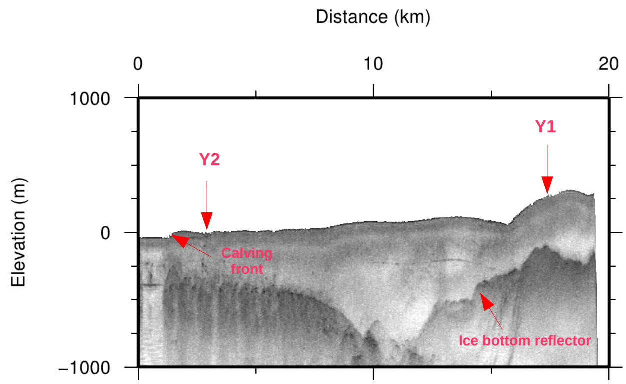

Fig. 7. Airborne radar profile corresponding to the Y1-Y2 profile of Fig. 8.

A compilation of floatation results for both ground and airborne data is shown in Fig. 8. The colors give the required density value for the ice slab to reach hydrostatic equilibrium above the ocean given the ice free board and the ice total thickness. From the chosen ice density of about $880\ \mathrm{kg.m^{-3}}$, (accounting for the possible presence of a firn layer as well as crevasses) a first guessed hydrostatic grounding line can be proposed as represented on the figure by the yellow dots. Assuming a density of $900\ \mathrm{kg.m^{-3}}$ in the present case would significantly reduce the floating shelf and require quite a lot of 'regrounding' within the basin. Although this possibility cannot be excluded (notably given the rough topography measured below the grounded parts of the glacier), the required amount of grounding appears incompatible with the surface displacements measured in our following kinematic approach. Local pinning points or even small grounded areas close to floatation remain however possible seaward of the proposed GL according to the computed density values (see question marks on the figure).

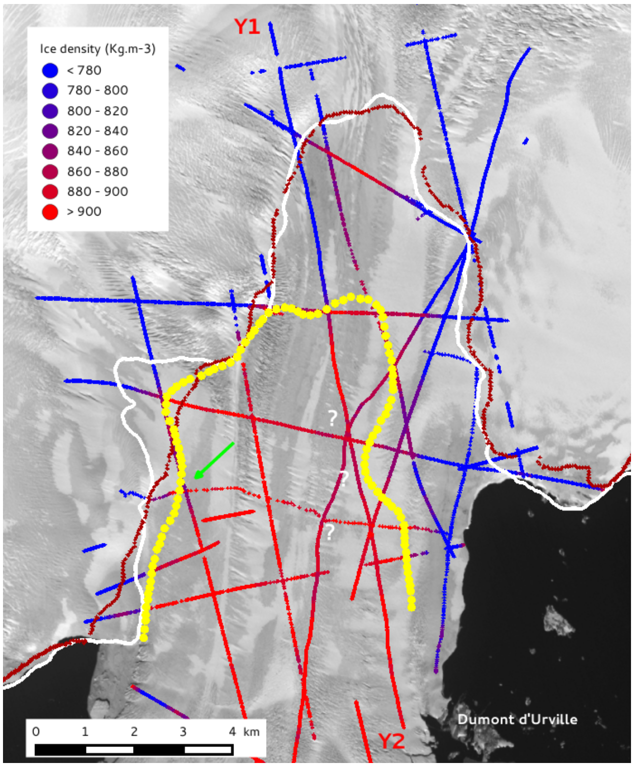

Fig. 8. Hydrostatically determined transitions between grounded (blue) and floating (red) ice along all radar profiles performed over the coastal part of the Astrolabe Glacier as a function of the chosen value for ice density. Assuming the central value of 880 $\mathrm{kg.m^{-3}}$ for the ice density a grounding line position is proposed under the form of the yellow line. The green arrow points towards the radar profile intersection where a large discrepancy in ice thickness is observable. Y1 and Y2 denote both ends of the radar profile of Fig. 7. Question marks indicate places of possible partial grounding (pinning points). The white and brown lines are the grounding lines as proposed by Bindschadler et al. (2011) and Scambos et al. (2007) respectively.

In fact, trying to adjust the column average density any further for the sake of refining an hydrostatically derived grounding line is useless at this stage because (i) this density varies laterally along the profiles, (ii) errors on the radar depths have to be considered and (iii) the hydrostatic approach remains approximative. If on the one hand ground radar depths are reliable, airborne ones are subject to much larger uncertainties mainly resulting from the measurement method itself. Indeed, the radar beam spot at the basal interface ranges from 1 km across for the VHF to several km for the MF system so that any rough topography in that spot can appear to map directly below the aircraft. As a consequence, a RMS of $50\ \mathrm{m}$ for this depth offset is common which leads to some of the observed discrepancies . This is confirmed by crossing points between ground and airborne profiles which often show large discrepancies. For instance the crossing outlined by the green arrow (Fig. 8) shows significantly different inferred density values resulting from radar ice thicknesses of 390 and 680 m for the airborne and ground radar respectively. As a consequence, when outlining our so-far proposed grounding line by using the central ice density value of $880\ \mathrm{kg.m^{-3}}$, preference was given to ground radar data when they were conflicting with airborne ones.

Inspection of Figure 8 shows various shifts of the floatation point when the chosen density varies. One transition color represents a $20\ \mathrm{kg.m^{-3}}$ density change which can more or less be considered as the uncertainty on the ice column average density value. These shifts are generally limited on the sides of the fjord because of rather steep slopes there (the width of a color being of the order of 250 m in most cases) but can significantly increase up to $500\ \mathrm{m}$ to 1 km along flow as the result of less pronounced slopes. A RMS of 50 m on the airborne radar depths leads to an extra uncertainty which also depends on the slope of the bedrock. Figure 6 (ProfileI-J)shows that close to the grounding line, a $\pm 10\ \mathrm{kg.m^{-3}}$ change usually leads to a $\pm 50/100\ \mathrm{m}$ vertical shift of the floatation depth. As a consequence, the uncertainty resulting from errors on radar depths can be assumed to be of the same order as that from errors on density. We therefore end up with an overall uncertainty of about $1\ \mathrm{km}$ for the proposed grounding line location.

As for the hydrostatic method proposed here, it is inaccurate insofar as the rigid stresses are neglected (even if they are seriously reduced when considering the long-term interaction of the ice with the ocean). The remaining bending forces make the actual contact point G locally deviate from that obtained from an assumed hydrostatic equilibrium. The proposed grounding line should therefore be considered as a first approximative guess that needs to be constrained by the kinematic method for instance. Despite the associated uncertainties so far, significant deviations from previous mappings from surface feature identification (Bindschadler et al. (2011); Scambos et al. (2007)) are already noticeable, especially on the left flank of the glacier.

4 Kinematic GPS grounding line position

As an independent test of GL position, we used a ground based tidal method of detecting the presence or absence of tidally-induced vertical movements of the ice upper surface using kinematic GPS positioning. Profiles of individual measurement points were set up in both along flow and cross flow direction (see green dots on Figs. 4 and 9).

4.1 Field differential GPS survey

The method is here very similar to IceSAT repeat-track analysis (Brunt et al., 2010) as it consists of measuring the ice surface height at low and high tides and observe where the resulting 2 profiles diverge as a result of tidal movement. Tidal amplitude in the sector is ~ 1 m (see Fig. 10). As ice shelf vertical displacements are damped by the rigid behaviour of the ice slab confined within a narrow embayment, the method requires a high accuracy in the measurements of the resulting limited vertical displacements of the ice surface. We here used dual carrier-phase differential GPS measurements as in Vaughan (1995). A reference GPS receiver was set up on the nearest rock outcrop, while a rover unit was used to acquire positions according to the 'Stop and Go' method over the successive points constituting the profiles (Fig. 9). The corresponding baseline was short enough (15 km at the most) so as to ensure real time radio transmission of appropriate corrective terms (mostly ionospheric and atmospheric delays) from the reference to the rover and to allow for kinematic ambiguity resolution with 'stop' recording phases not exceeding 30 seconds. Each of the measured points was precisely marked on the ground (using paint) in order for the second measurement to be performed at exactly the same place some 12 hours later. Accurate reoccupation was vital as the small-scale roughness of the glacier surface is such that moving half a meter is enough to change the surface height by as much as several tens of cm.

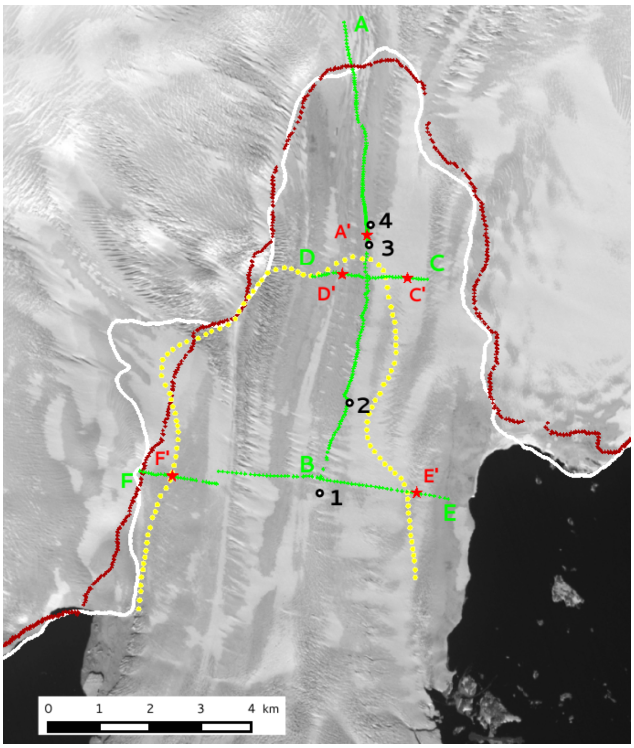

Fig. 9. Profiles made of measurement points (green dots) at which difference in ice upper altitude between high and low tides has been measured by GPS. Also featured is the grounding line preceding estimation. Red crosses (labelled A',C',D, E' and F') represent the transition points where this difference becomes significant (see text in Sect. 4.2.1) and points 1 to 4 the points where GPS have been dropped and have been recording continuously during several tidal cycles (Sect. 4.2.2).

4.2 Time-dependent ocean tides

The planning of the GPS surveys was dictated by the need for targeting highest and lowest tides. Unfortunately, the tide gauge at the nearby Dumont d'Urville station was not operational and we therefore had to rely on a prediction model (courtesy of Benoît Legrésy, see also Legrésy et al. (2004)). Fig. 10 shows the model predictions for the tides of January 2011.

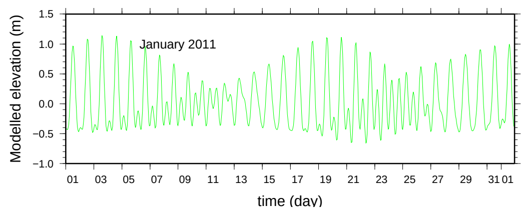

Fig. 10. Modelled tides for January 2011 where semi-dirurnal, diurnal and fortnighlty tidal periods are observable

This model was tested through our own ocean tide measurements. Vertical displacements of the nearby sea ice have been recorded for a couple of days and compared to the model results (Fig. 11). Despite a hardly perceptible discrepancy in the amplitudes, the phasing is perfect which allowed us to trust the model for planning our surveys and comparing our time-dependent surface height measurements to actual tides (as in Section 4.2.2).

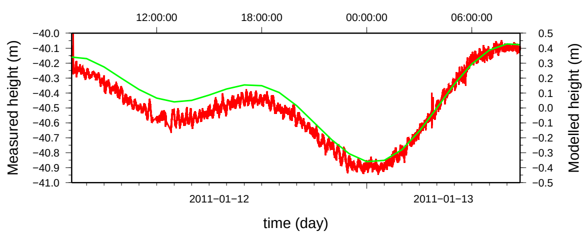

Fig. 11. Modelled (green) and measured (red) tides between the 12th and the 13th of January 2011. Surface displacements were measured on sea ice near the Astrolabe ice front by differential GPS with a baseline of less than 400 m allowing for very accurate measurements and a noise level of less than 5 cm.

4.2.1 Scaled profiles of time-differential elevation

Ice surface elevation along profiles [AB], [CD] and [EF] (Fig. 9) was measured at both high and low tides over chosen periods during which the tidal amplitude was as pronounced as possible. Measuring an entire profile (several hundred points) could sometimes last a couple of hours. Consequently, as mentioned by Vaughan (1995), the resulting profiles could not be considered as snap shots since the tide had time to evolve during the measurement period. Profiles were then scaled to the tidal amplitude e according to Eq. 5 of Vaughan (1995) :

$$d = \frac{e - e'}{p - p'} \tag{2}$$

where e, e', p, p' are surface elevation and tidal prediction at respectively high and low tides. As computed here d actually represents the observed tidal displacement normalized to tidal predictions and will hereafter be referred to as 'scaled displacement'.

This scaling is an indicator of the dampening in the ice surface displacements in response to the tidal forcing. Values below the unity express deviation from a fully hydrostatic response which results from the rigid bending of the ice slab. By spreading further out the actual water loading, vertical displacements just above the ocean are necessarily reduced so as to guarantee the overall force balance. This effect is all the more pronounced as the confinement is strong as can be seen from Figure 12 along the transverse EF profile where the floatation percentage only reaches 60% at the most in the middle. As a consequence, despite increasing along-flow displacements, floatation along the AB profile remains also limited and full recovery of tidal hydrostatism would require reaching the H point much further seaward out of the fjord. It should be recalled that these possibly large deviations from hydrostatism observed here only concern the response to the short-term tidal cycle and are not incompatible with an average longer-term ice slab ocean interaction much closer to hydrostatic equilibrium. Profile [AB] (Fig. 12, top) shows the ice surface altitude profile along flow and the elevation difference between low and high tides. This difference overcomes the GPS noise (here estimated to 15 cm) at about 4000 m along the profile (Fig. 12, top; black vertical line). According to Section 1 and Fig. 3, this distance corresponds to point X somewhere between points F and G. The required shifting of X from F towards G depends on the accuracy of the kinematic method when the height difference becomes significant above the noise level (from 15 up to 20 to 30 cm depending on the GPS data quality).

Interestingly, an inflexion in the amplitude of the tidal movement is observable at a distance of 7000 m from the start of the profile and shows consistency with the hydrostatic GL getting closer (at the level of GPS drop point 2 which actually lies 7500 m from point A, see Fig. 9). Further downstream scaled displacements increase again and appear compatible with an hydrostatic GL that moves away. This can be seen as an illustration of surface displacements getting closer to full tidal movement as one moves away from the GL.

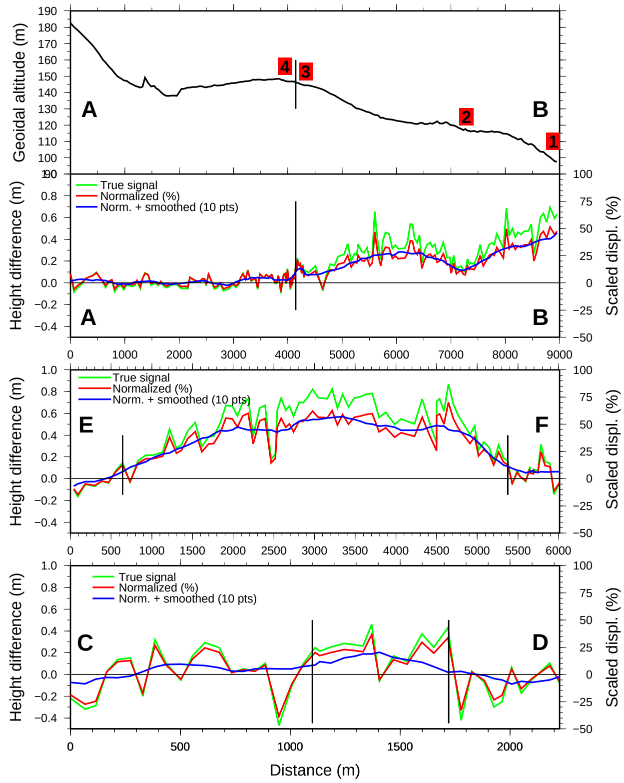

Fig. 12. Difference in ice surface altitude between high and low tide for profile [AB], [EF] and [CD]. The green curve represent true GPS data difference, whereas the red one represents this difference scaled to the tidal amplitude (expressed in percentage). The blue line is a smoothing (over 10 points) of the red curve. Locations where the altitude difference becomes significant are featured by the black vertical line and define our grounding line kinematic control points. The altitude above sea level for profile [AB] is also displayed on top along with the positions of the 4 GPS drop points along the profile (see Sect. 4.2.2)

It will be seen in Section 4.2.2 that these scaled displacement are also consistent with the time-dependent GPS measurements of the ice surface at GPS drop points 1 to 4. It is therefore possible at this stage to anticipate a more seaward GL than the so far obtained spaceborne ones (Scambos et al., 2007; Bindschadler et al., 2011) on the western margin of the glacier. Similar interpretation over profile [EF] allowed for determination of 2 extra control points from the same GPS noise level. Conversely, data for profile [CD] was more noisy due to a poor satellite GPS constellation during one of the transects. Despite an uncertainty of at least 20 to 30 cm, a difference between high and low tide profiles is perceptible and has finite vertical displacements in the central part. Although the proposed positioning for the 2 resulting control points remains questionable over this specific profile, the presence of an uplifted central zone is confirmed by a time-dependent tidal signal (see Sect. 4.2.2) already detectable at

GPS drop point 3 upstream of the [CD] profile (Fig. 13). The resulting 5 points obtained in this way along the 3 GPS profiles thus represent 5 control points for the positioning of our kinematic GL and are displayed as red stars on Fig. 9 along with the proposed hydrostatic positioning.

4.2.2 Time-dependent tidal measurements

We confirm these results with continuously measured surface displacements with GPS receivers placed on the ground for several days and recording in the differential mode. Four drop points (Point 1 to Point 4) were selected along the profile [AB] (Figs. 4, 9, Fig. 12, top) and corresponding surface vertical displacements displayed on Figs. 13 and 14. Point 1 is roughly situated in the middle of Profile [EF] and at the extremity of profile [AB] and shows a clear tidal signal whose amplitude is 55% of the predicted tidal range, consistent with the scaled altitude differences found on Fig. 12. There is a small shift in phase, with the shelf responding with a time lag of the order of one hour. A possible explanation for the phase offset is the propagation offset of the tidal signal from the open ocean to grounding zone through the ice shelf cavity. A small anelastic component in the ice deformation is also possible as ice exhibits a visco-elastic behaviour at tidal periods (Gudmundsson, 2011).

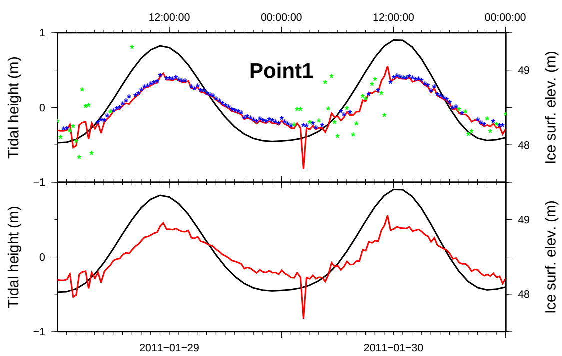

Fig. 13. Time-dependant surface displacements during 2 days in january 2011 at Point 1. On the bottom panel are shown the tidal signal (black) compared to the vertical ice upper surface displacements obtained in RTK differential mode (red). GPS data were also post-processed so as to confirm the validity of the RTK method. Corresponding results are depicted as blue stars (upper panel) when ambiguities where fixed and as green stars otherwise. The consistency between the red curve and the set of blue dots confirms the validity of the RTK approach whose results are then later systematically used in Fig. 14.

At point 2, a phasing is still visible but the amplitude is here reduced (about 20% to 25% of the tidal amplitude as also observable on profile AB at the distance of 7500 m from point A) indicating the proximity of the GL less than a km westward. Point 3 requires a vertical exaggeration to exhibit a phasing that just overcomes the GPS noise level whereas no tidal signal is detectable anymore at point 4. Again, according to the respective positions of these last 2 points along profile AB (4000 m and 4400 m) such results appear fully compatible with the scaled displacements as depicted on top of Fig. 12 and justify the positioning of the kinematic control point just in between. Moreover, Point 3 exhibiting limited upper surface displacements despite being located upstream of the hydrostatic GL illustrates the specific behaviour over the F-G distance as represented in Figs 3 and 15. This point is either partially lifted from ground during high tides (lying between G and G_H) or permanently stuck to it (between F and G_H), but is not considered as floating in our 'hydrostatic' sense of the meaning.

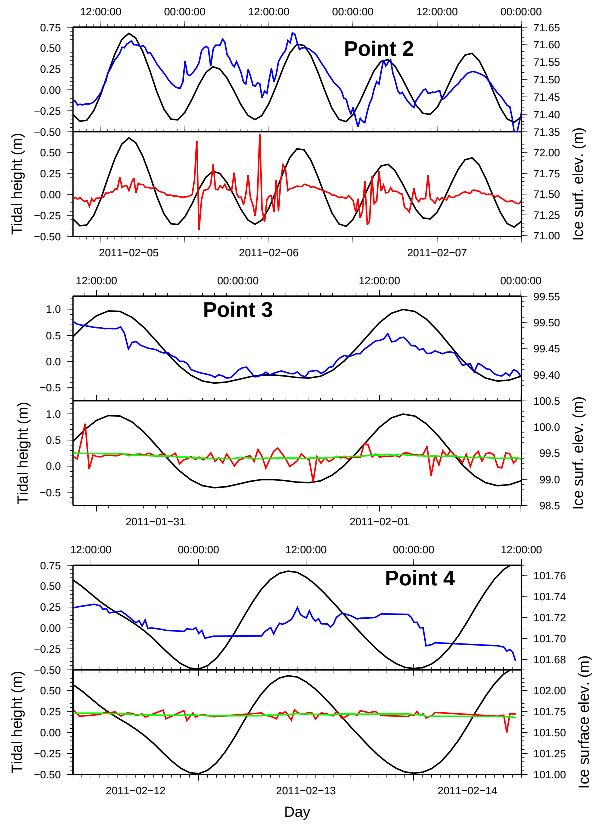

Fig. 14. Comparison of the upper surface displacements and tides for Point 2, 3 and 4. Black curves represent the tidal amplitude whereas the red ones stand for raw RTK GPS positions. Blue curves result from a 10-point smoothing of the raw data to which a vertical amplification has been applied (varying according to the point) in order to confirm or deny any correlation with the tides. Green curves for points 3 and 4 just represent the smoothing of raw GPS data.

5 Elastic plate modelling

Inspection of Fig. 9 shows kinematic control points very close to their hydrostatic counterparts. This however can be considered as a coincidence since the measured points do not represent the same objects/and or processes as can be seen from Fig. 15. The figure here notably shows how surface points from the outer fringe (between F and G) can rise under the tidal forcing with their base still more or less in contact with the bedrock (probably like Point 3 for instance). By exhibiting a signal just above the GPS noise threshold, GPS point 3 probably stands around the X position upstream of the hydrostatic GL. The consistency of the two methods actually depends on the X-G distance as represented on the figure, which will in turn depend on both the regional rigid bending of the ice (F-G distance, see Section 5) and the accuracy for the kinematic method. F-G distances of the order of $0.5\ \mathrm{km}$ to $1\ \mathrm{km}$ have been reported for Petermann Glacier in Greenland (Rignot et al. (2011)), but there is no indication as to why they would apply in the present case.

This is why modelling the tidally-induced rigid behaviour of the ice slab is an independent way of assessing this distance and therefore deducing this degree of consistency. The elastic response of the glacier to the tidal push within the fjord is computed and corresponding results analysed in terms of (i) ice slab thickness and (ii) size of the loading pattern. The F-G distance is the result of the rigid behaviour of the plate contrary to a local response where the two points would overlap. It is well known that deviation from a local hydrostatic equilibrium for a rigid slab is a function of both its flexural strength (proportional to its thickness raised at the third power) and, to a lesser degree, to the spatial extent of the load (e.g., Le Meur, 2001). In this case, the latter effect is forced by the narrowness of the fjord, which prevents the ice from exhibiting full floatation with respect to the tidal forcing (see section 4.2.1). The shape of the fjord as far as it can already be assessed from the preliminary outlining of the grounding line (as represented on Figs. 8 and 9) shows a varying width ranging from $5\ \mathrm{km}$ to $1\ \mathrm{km}$. Last, because the 2-D model as used here can only deal with a uniform thickness, sensitivity tests are also performed with regards to the thickness of the plate.

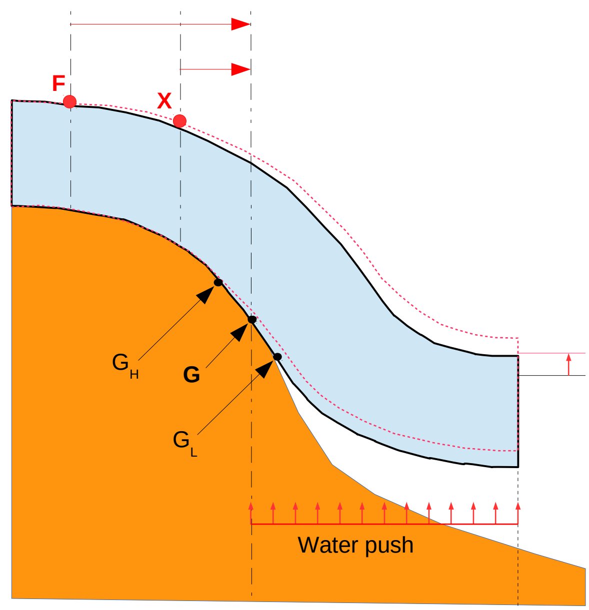

Fig. 15. Hydrostatically-balanced ice slab in the low-tide position onto which is then applied a water push (featured as the red arrows) leading to the high tide configuration (dashed lines). G_L and G_H respectively denote the low and high-tide grounding lines with G the average position here placed in the middle and corresponding to our hydrostatic position. F is the landward limit of tidal upper displacements and X a seaward point where the uplift becomes significant enough to overcome the noise threshold of the chosen kinematic method. Top red arrows represent the F-G and F-X distances. Of importance is to notice that the part of the slab situated between points F and G (theoretically G_H) can possibly undergo surface movements whereas still in contact with the bedrock as the result of the tidal bending moment of the ice slab.

5.1 Elastic plate theory

The 2-D elastic bending in response to a point load q of a rigid elastic plate floating over an inviscid fluid of density ρ_w is given by the following constant coefficient differential equation of Brotchie and Silvester (1969) in which the momentum due to the Earth curvature can be neglected :

$$D\nabla^4 w + \rho_w g w = q \tag{3}$$

where w is the downward deflection, ∇ the 2-D gradient operator and D the flexural rigidity of the plate given by :

$$D = \frac{EH^3}{12(1-\nu^2)} \tag{4}$$

with E the Young elastic modulus taken equal to $0.9\ \mathrm{GPa}$ (Vaughan, 1995) , ν the Poisson coefficient (0.3) and H the plate thickness. The term $\rho_w g w$ represents the buoyancy force resulting from the downward displacement w within the fluid. As a consequence, the water push forcing resulting from a tidal amplitude of δm can be expressed as $\rho_w g \delta$ which in the absence of surface load ($q = 0$) leads to :

$$D\nabla^4 w + \rho_w g(w + \delta) = 0 \tag{5}$$

Solution to a point load q is a deflection profile as a function of the scaled distance $r = x/L_r$, x being the true distance and $L_r = (\frac{D}{\rho_w g})^{1/4}$ a flexing width. It reads :

$$w(r) = \frac{q}{2\pi\sqrt{D\rho_w g}} kei(r) \tag{6}$$

where q is here a 'negative' load (corresponding to the ocean push) equal to $-\rho_w g \delta$ and kei the Kelvin function of zeroth order. Since the elastic bending of a rigid plate is a linear process with respect to the load, the actual response to a realistic load reads as the sum of the contributions of all the points that constitute the loading pattern. The plate deformation finally expresses under the form of the spatial convolution of that load distribution with the 'unit response' as given by Eq. 6.

5.2 Experimental set up

In the present simulation, the domain has been digitized on a $100\ \mathrm{m} \times 100\mathrm{m}$ grid representing a 12 by $10\ \mathrm{km}$ rectangle over which different loading patterns are tested. The pattern of the load (water push) is here featured as a simple fjord with parallel walls and terminating under the form of a semi-circular shape whose radius is half the width between the walls (see Fig. 16). We here consider the ice resting on a low-tide ocean and then undergoing a water upward displacement of $1\ \mathrm{m}$ corresponding to the tidal amplitudes when field measurements were carried out. The outward limit of the load (red line on the figure) is meant to match the hydrostatic grounding line as depicted on Fig. 15. Different shapes are tested with a terminal radius ranging from $500\ \mathrm{m}$ to $5\ \mathrm{km}$ as represented in green in the bottom part of Fig. 16 (implying fjord widths from 1 to $10\ \mathrm{km}$). The figure shows the case of the elastic rigid bulging of a 800-m thick ice slab in response to a 1-m water push over the 5-km wide fjord here displayed in red.

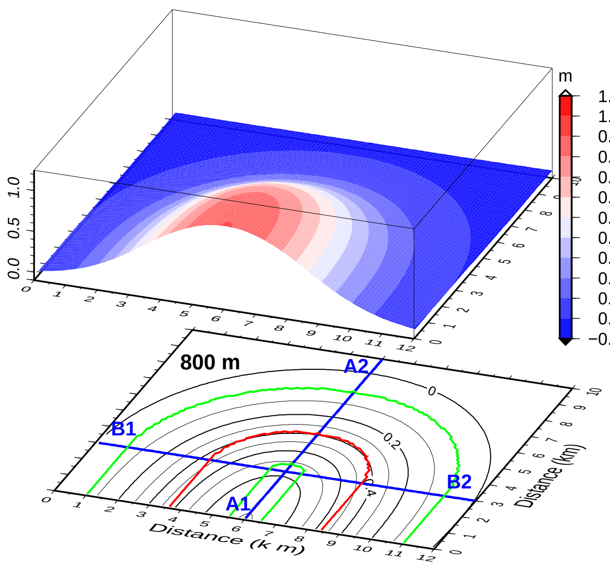

Fig. 16. Elastic bulging of a 800-m thick ice slab (upper part) in reponse to a 1-m bottom water push exerted over the domain as outlined in red (bottom part). Green contours show the two extreme fjord geometries of the sensitivity test (see Fig. 18) whereas the black ones are the deformation contours corresponding to the 3-D upper view. Aslo outlined are the two cross sections represented in Fig. 17

5.3 Results in terms of deviation from hydrostatic equilibrium

We find that the surface response is not local, extending beyond the limits of the underlying water push. Deviation from a local (hydrostatically equilibrated) deformation can be assessed from the spacing between the 0-deformation contour and the outline of the load. Cross sections (Fig. 17) offer a clear estimation of this rigid behaviour expressed by the shift between the termination of the load (hydrostatic point G) and the actual point of zero deformation. More specifically, the G-X distance is here deduced from the intersection with the $0.15\ \mathrm{m}$ ice surface uplift (green line) corresponding to our estimated GPS detection threshold.

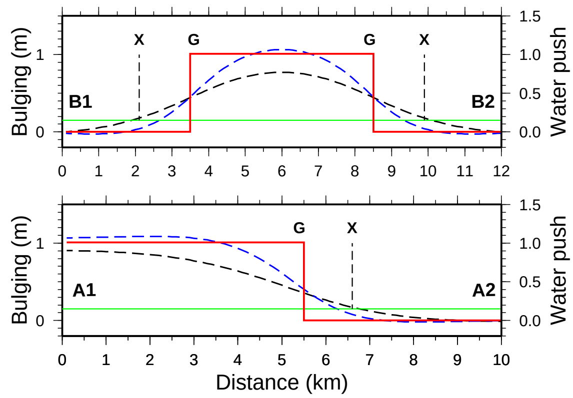

Fig. 17. Longitudinal and orthogonal cross sections of both the loading pattern (red) and corresponding ice surface uplift (black) along profiles A1-A2 and B1-B2 of Fig. 16. The green horizontal line represents the surface smallest displacement of $0.15\ \mathrm{m}$ detectable by the kinematic GPS measurements. Full floatation implies a 1-m uplift as is almost the case on the left part of the A1-A2 profile (mouth of the fjord). The blue curve shows the same deflection profiles obtained with an elastic modulus ten times smaller than the previously adopted value of $0.9\ GPa$ (Vaughan, 1995). The water push is here expressed as the weight exerted over each cell of the domain ($100 \times 100 \times \rho_w g \delta$) in 10^8 Kg

We note that the chosen example with a 5 km-wide fjord more or less matches the configuration along profile IJ (Fig. 5) and agrees with partially free floating ice on the cross profile as was actually measured. However, the model gives a central displacement 75% that of the tide whereas measurements are only 50 to 60%. The suspected nearby ice plain close to drop point 2 where the GL comes closer to the profile (Fig. 9, not accounted for in the model) is likely responsible and would explain such a discrepancy . The main weakness of the proposed model comes from its inability to account for a varying thickness of the slab (whereas this latter varies from $400\ \mathrm{m}$ to $1000\ \mathrm{m}$ along the IJ profile). Rather than trying to (improperly) reproduce a given configuration, it was instead decided to span a whole range of values for both the ice thickness and the loading shape that are to be expected over the glacier so as to assess the corresponding orders of magnitude for the G-X distance.

Corresponding results are displayed on Fig. 18, where the G-X distance is depicted as a function of both the plate thickness and the semi width of the ocean forcing (curvature of the terminating fjord). The figure shows limited G-X distances when the plate thickness is small whatever the size of the load. It is simply the result of a shorter flexing width when the overall rigidity of the plate is reduced. Similar G-X distances are also found with a thicker slab if the load remains limited. In this latter case, the shortness is due to the small-sized load to which the rigid plate responds with small vertical displacements. Only large-scale loads associated with a thick ice slab lead to significant G-X distances.

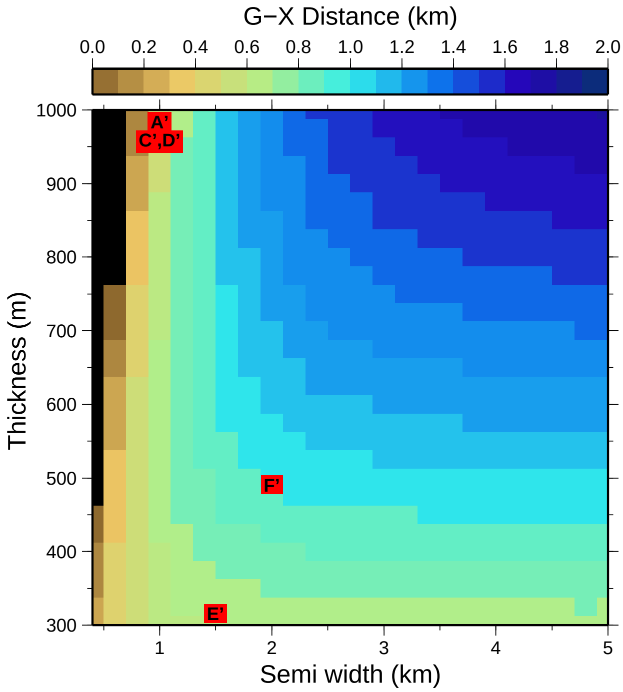

Fig. 18. G-X distance (km) as a function of the ice slab thickness and the semi width of the forcing pattern. The five kinematic GPS control points A', C', D', E' and F' are here placed according to their specific parameter combinations. For display purpose, point A' (1050 m ice thickness) had to be lowered to 975 m.

6 Consistency of the hydrostatic and kinematic approaches

The consistency between the hydrostatic and the GPS kinematic methods can now be assessed by positioning each of the 5 GPS control points within the parameter space (size of the load / ice thickness) and estimating the corresponding G-X distance. From the surface heights, assuming floatation, a good estimation of the ice thickness can be derived for points A',C',D',E',F' which respectively gives 1050, 950, 950, 325 and 500 m (control point being here labelled according to the kinematic GPS profiles). As for the size of the tidal water push pattern, given the presumed shape of the underneath fjord as featured in Figs 8 and 9, a semi width of 1 km can be associated to the upstream A', C' and D' control points. For downstream points, a fjord semi width of some 2 km seems relevant for control point F' on the right flank of the glacier.As for point E', the nearby inflexion of the hydrostatic GL to the South East (Fig. 8) led us to reduce the loading curvature and adopt a value down to 1.5 km. The resulting parameter combinations (see their positions in Fig. 18) yield G-X distances of about 600 m for the A',C' and D' points, a distance of some 900 m for point F' and finally a distance of 750 m for point E'. According to Fig. 16, the hydrostatic GL should lie seaward of the GPS control points with an offset theoretically equal to these respective distances along the GPS profiles. The computed offsets are consistent for points A' and C' whereas D' is apparently on the wrong side. However, as said earlier, the positioning of points C' and D' remains questionable. Point F' should be offset by 900 m but actually lies on the hydrostatic GL. Such a result however fits within the previously estimated uncertainty of 1 km for the hydrostatic positioning of the GL. Moreover, uncertainties on the model results can not be discarded and the computed distances should be considered as orders of magnitude. In particular, the flexing length appears very sensitive to the elastic modulus as can be seen from Fig. 17 where a 10 times smaller modulus yields twice as small X-G distances. Adopted values for an ice-shelf elastic modulus are sparse as can be seen from the literature (span several orders of magnitude, see for example Table-1 in (Vaughan, 1995)), and using a smaller value is a way of accounting for the anelastic part of the deformation under the form of a partial visco-elastic behaviour occurring even at tidal frequencies. Finally, for point E', the actual shift of 300 m is below the computed value, but this latter could as well be less with a lower elastic modulus and anyway remains within the uncertainty for the hydrostatic GL.

As a consequence, rather than telling where the GL exactly stands, the modelled orders of magnitude show the consistency between the kinematic and the hydrostatic approaches. The hydrostatic line as outlined in Figs. 8 and 9 can therefore be considered as a good representation of the grounding line to within its associated uncertainty of a km or so. The discrepancy with those of Bindschadler et al. (2011) and Scambos et al. (2007) is in some place much larger than this possible error and can be as much as several km, especially in the upper part and over the left flank of the glacier. The automated used for targeting surface topographic specific features (Bindschadler et al., 2011) or the large-scale filtering procedures sometimes corrupting upper surface topographic signatures (Scambos et al., 2007) lead to additional uncertainty. Close inspection of the SPIRIT DEM reveals that these two proposed grounding lines often cross areas where the surface exhibits a convex shape rather than the concave one expected in the vicinity of the break in slope (especially on the left flank of the glacier, see Fig. 4). Last, the ASAID and MOA grounding lines are far from the hydrostatic condition. The SPIRIT DEM gives an altitude of 130 ma.s.l. at the inland extremity of the QR radar profile (point R) which overlaps with the two grounding lines. Assuming floatation there, a simple hydrostatic calculation (with ρ_w and ρ_i respectively equal to $1028\ \mathrm{kg.m^{-3}}$ and $890\ \mathrm{kg.m^{-3}}$) would give an ice thickness of $970\ \mathrm{m}$ which strongly conflicts with that of $200\ \mathrm{m}$ inferred from the ground GPR survey (see Fig. 5).

7 Conclusions

The methods as described here represent two independent means of mapping the grounding line of a coastal glacier like the Astrolabe Glacier. Our study first shows that because of decoupled processes operating at different time scales, the line of uppermost surface tidal displacements does not match that of bedrock contact points resulting from the essentially hydrostatic long term interaction of the ice with the ocean. However, it is found that under most conditions prevailing over such small glaciers like the Astrolabe (size of the fjord, thickness of the ice), the offset between the two remains limited and barely exceeds 1 km. Moreover, the GPS kinematic method maps points which are actually closer to their hydrostatic counterparts because the uncertainty of the method requires a detection threshold to be overcome which leads to a seaward shift. Both radar and GPS measurements presented here tend to confirm this consistency. Indeed, GPS measurements once corrected according to the results of a 2-D elastic plate deformation suggest a grounding line that remains within the error bars of the hydrostatic approach that comprise uncertainties on both the ice density and the radar measurements.

Our final result is a grounding line that is significantly more seaward than those determined by Bindschadler et al. (2011) and Scambos et al. (2007). So far, no other grounding line has been proposed over the area. In these static studies, the GL is exclusively based on surface topographic features (like the break in slope for instance). If for large-scale glaciers or ice shelves the difference between this surface signature and the actual grounding line is rather limited compared to the size of the ice bodies (as can be seen from the comparison with ICEsat or InSAR data in Scambos et al. (2007) for instance), this difference can rapidly become of the order of the glacier typical size for smaller bodies like the Astrolabe Glacier where differences can locally reach 3 to $4\ \mathrm{km}$.

For glaciers larger than the Astrolabe, the inconsistency between the two approaches used in the present study might become more pronounced. Indeed, larger ice thicknesses associated with larger tidal loading patterns will yield enhanced rigid deviations (G-F distances). Mapping the grounding line assuming hydrostatic equilibrium from both lower and upper ice surfaces measurements (which are nowadays widely available from airborne campaigns) remains reliable as long as the associated uncertainties are kept low. If bedrock slopes are steep as is the case with the Astrolabe, lateral shifts of the grounding line due to these errors are minimized. On the other hand, if the potentially more accurate kinematic approaches (GPS, satellite altimetric data...) have to be used, proper correction of the 'elastic plate effect' can be critical as the glacial system is large. In such a case, a 3-D elastic plate modelling allowing for spatially changing ice thicknesses should ideally be considered.

Acknowledgements. This study was funded by the **A**gence **N**ationale pour la **R**echerche (ANR) through the DACOTA project No. **ANR-06-VULN-016-01** and the "ADAGE " project No. **ANR-09-SYSC-001**. Field activities described here largely benifited from logistical and financial support from the French polar **I**nstitute **P**aul **E**mile **V**ictor (IPEV). E. Berthier acknowledges support from the French Space Agency (CNES) through the TOSCA and ISIS proposal #580. ICECAP operations over Astrolabe Glacier were funded by NASA's Ice Bridge program (**NNX09AR52G** and **NNX11AD33G** to the University of Texas at Austin); WISE was funded by a grant from NASA's IPY program to the Jet Propulsion Laboratory. This work has also been supported by a grant from LabEx OSUG@2020 (Investissements d'avenir - ANR10LABX56). Constructive comments and suggestions from two anonymous reviewers have been very helpful in improving this paper.

References

Bamber, J. and Bentley, C.: A comparison of satellite-altimetry and ice-thickness measurements of the Ross Ice Shelf, Antarctica, Annals of Glaciology, 20, 357-364, 1994.

Bindschadler, R., Choi, H., Wichlacz, A., Bingham, R., Aberdeen, A. B., Bohlander, J., Brunt, K., Corr, H., Drews, R., Fricker, H., et al.: Getting around Antarctica: new high-resolution mappings of the grounded and freely-floating boundaries of the Antarctic ice sheet created for the International Polar Year, The Cryosphere, 5(3), 569-588, 2011.

Brotchie, J. F. and Silvester, R.: On crustal flexure, Journal of Geophysical Research, 74, 5240-5252, 1969.

Brunt, K. M., Fricker, H. A., Padman, L., Scambos, T. A., and O'Neel, S.: Mapping the grounding zone of the Ross Ice Shelf, Antarctica, using ICESat laser altimetry, Annals of Glaciology, 51, 71-79, 2010.

Corr, H. F. J., C. S. M. Doake, A. Jenkins, and D. G. Vaughan, Investigations of an ice-plain in the mouth of Pine Island Glacier, Antarctica, Journal of Glaciology, 47, 51-57, 2001.

Craven, M., Carsey, F., Behar, A., Matthews, J., Brand, R., Elcheikh, A., Hall, S., and Treverrow, A.: Borehole imagery of meteoric and marine ice layers in the Amery Ice Shelf, East Antarctica, Journal of Glaciology, 51, 75-84, 2005.

Depoorter, M. A., Bamber, J. L., Griggs, J. A., Lenaerts, J. T. M., Ligtenberg, S. R. M., van den Broeke, M. R. and Moholdt, G.: Calving fluxes and basal melt rates of Antarctic ice shelves, Nature, 502, (7469), 89-92, 2013

Durand, G., Gagliardini, O., Zwinger, T., Le Meur, E., and Hindmarsh, R.: Full Stokes modeling of marine ice sheets: influence of the grid size, Annals of Glaciology, 50, 109-114, 2009.

Fricker, H. A. and Padman, L.: Ice shelf grounding zone structure from ICESat laser altimetry, Geophys. Res. Lett., 33, (15), 2006.

Fricker, H. A., Popov, S., Allison, I., and Young, N.: Distribution of marine ice beneath the Amery Ice Shelf, Geophys. Res. Lett., 28, (11), 2241-2244, 2001.

Gagliardini, O., Durand, G., Zwinger, T., Hindmarsh, R. C. A., and Le Meur, E.: Coupling of ice-shelf melting and buttressing is a key process in ice-sheets dynamics, Geophysical Research Letters, 37, (14), 2010.

Goldstein, R. M., H. Engelhardt, B. Kamb, R. M. Frolich: Satellite Radar Interferometry for Monitoring Ice Sheet Motion: Application to an Antarctic Ice Stream, Science, 3, (5139), 1525-1530, 1993

Gudmundsson, G. H.: Ice-stream response to ocean tides and the form of the basal sliding law, The Cryosphere, 5, 259-270, 2011.

Horgan, H. J. and Anandakrishnan, S.: Static grounding lines and dynamic ice streams: Evidence from the Siple Coast, West Antarctica, Geophys. Res. Lett., 33, (18), 2006.

Joughin, I. and Padman, L.: Melting and freezing beneath Filchner-Ronne Ice Shelf, Antarctica, Geophys. Res. Lett., 30, (9), 2003.

Joughin, I. R., Kwok, R., and Fahnestock, M. A.: Interferometric estimation of three-dimensional ice-flow using ascending and descending passes, IEEE Transactions on Geoscience and Remote Sensing, 36, 25-37, 1998.

Korona, J., Berthier, E., Bernard, M., Rémy, F., and Thouvenot, E.: SPIRIT. SPOT 5 stereoscopic survey of Polar Ice: Reference Images and Topographies during the fourth International Polar Year (2007-2009), ISPRS Journal of Photogrammetry and Remote Sensing., 64, (2), 204-212, 2009.

Legrésy, B., Wendt, A., Tabacco, I., Rémy, F., and Dietrich, R.: Influence of tides and tidal current on Mertz Glacier, Antarctica, Journal of Glaciology, 50, 427-435, 2004.

Le Meur, E.: Effects of a viscoelastic lithosphere on the isostatic bedrock response, Earth and Planetary Science Letters, 188, 221227, 2001.

Pattyn, F., Huyghe, A., De Brabander, S., and De Smedt, B.: Role of transition zones in marine ice sheet dynamics, Journal of Geophysical Research: Earth Surface 111, F2, 2006.

Rignot, E.: Hinge-line migration of Petermann Gletscher, north Greenland, detected using satellite radar interferometry, Journal of Glaciology, 44, (148), 1998.

Rignot, E. and Jacobs, S. S.: Rapid bottom melting widespread near Antarctic ice sheet grounding lines, Science, 296, 2020-2023, 2002.

Rignot, E., Mouginot, J., and Scheuchl, B.: Antarctic grounding line mapping from differential satellite radar interferometry, Geophys. Res. Lett., 38, (10), 2011.

Robin, G., C. S. M. Doake, H. Kohnen, R. D. Crabtree, S. R. Jordan, and D. Moller, Regime of the Filchner-Ronne ice shelves, Antarctica, Nature, 302, (5909), 582586, 1983.

Scambos, T. A., Haran, T. M., Fahnestock, M. A., Painter, T. H., and Bohlander, J.: MODIS-basedh Mosaic of Antarctica (MOA) data sets: Continent-wide surface morphology and snow grain size, Remote Sensing of Environment, 111, 242-257, 2007.

Schoof, C.: Ice sheet grounding line dynamics: Steady states, stability, and hysteresis, Journal of Geophysical Research: Earth Surface 112, F03S28, 2007.

Shepherd, A. et al.: A Reconciled Estimate of Ice-Sheet Mass Balance, science, 338, 1183-1189, 2012.

Van der Veen, C. J.: Fracture mechanics approach to penetration of surface crevasses on glaciers, Cold Regions Science and Technology, 27, 31-47, 1998.

Vaughan, D.: Tidal flexure at ice shelf margins, Journal of Geophysical Research, 100, 6213-6224, 1995.

Vaughan, D. G., Corr, H. F. J., Bindschadler, R. A., Dutrieux, P., Gudmundsson, G. H., Jenkins, A., Newman, T., Vornberger, P., and Wingham, D. J.: Subglacial melt channels and fracture in the floating part of Pine Island Glacier, Antarctica, Journal of Geophysical Research, 117, (F3), 2012.

Wen, J., Jezek, K. C., Csath, B. M., Herzfeld, U. C., Farness, K. L., and Huybrechts, P.: Mass budgets of the Lambert, Mellor and Fisher Glaciers and basal fluxes beneath their flowbands on Amery Ice Shelf, Science in China Series D: Earth Sciences, 50, 1693-1706, 2007.

Wen, J., Wang, Y., Wang, W., Jezek, K. C., Liu, H., and Allison, I.: Basal melting and freezing under the Amery Ice Shelf, East Antarctica, Journal of Glaciology, 56, 81-90, 2010.

Young, D. A., A. P. Wright, J. L. Roberts, R. C. Warner, N. W. Young, J. S. Greenbaum, D. M. Schroeder, J. W. Holt, D. E. Sugden, D. D. Blankenship, T. D. van Ommen, and M. J. Siegert, A dynamic early East Antarctic Ice Sheet suggested by ice covered fjord landscapes, Nature, 474, 7275, 2011.

Zwally, H. J., Giovinetto, M. B., Li, J., Cornejo, H. G., Beckley, M. A., Brenner, A. C., Saba, J. L., and Yi, D.: Mass changes of the Greenland and Antarctic ice sheets and shelves and contributions to sea-level rise: 19922002, Journal of Glaciology, 51, 509-527, 2005.